

## ARTICLE OPEN



# ENSO skewness hysteresis and associated changes in strong El Niño under a CO<sub>2</sub> removal scenario

Chao Liu<sup>1</sup>, Soon-Il An<sup>1,2,3</sup>✉, Fei-Fei Jin<sup>4</sup>, Malte F. Stuecker<sup>5</sup>, Wenjun Zhang<sup>6,7</sup>, Jong-Seong Kug<sup>3,8</sup>, Xinyi Yuan<sup>9,10</sup>, Jongsoo Shin<sup>3</sup>, Aoyun Xue<sup>3</sup>, Xin Geng<sup>3,6,7</sup> and Soong-Ki Kim<sup>1</sup>

El Niño–Southern Oscillation (ENSO) sea surface temperature (SST) anomaly skewness encapsulates the nonlinear processes of strong ENSO events and affects future climate projections. Yet, its response to CO<sub>2</sub> forcing remains not well understood. Here, we find ENSO skewness hysteresis in a large ensemble CO<sub>2</sub> removal simulation. The positive SST skewness in the central-to-eastern tropical Pacific gradually weakens (most pronounced near the dateline) in response to increasing CO<sub>2</sub>, but weakens even further once CO<sub>2</sub> is ramped down. Further analyses reveal that hysteresis of the Intertropical Convergence Zone migration leads to more active and farther eastward-located strong eastern Pacific El Niño events, thus decreasing central Pacific ENSO skewness by reducing the amplitude of the central Pacific positive SST anomalies and increasing the scaling effect of the eastern Pacific skewness denominator, i.e., ENSO intensity, respectively. The reduction of eastern Pacific El Niño maximum intensity, which is constrained by the SST zonal gradient of the projected background El Niño-like warming pattern, also contributes to a reduction of eastern Pacific SST skewness around the CO<sub>2</sub> peak phase. This study highlights the divergent responses of different strong El Niño regimes in response to climate change.

*npj Climate and Atmospheric Science* (2023)6:117; <https://doi.org/10.1038/s41612-023-00448-6>

## INTRODUCTION

El Niño–Southern Oscillation (ENSO) is an air–sea coupled phenomenon occurring in the equatorial Pacific with pronounced climatic impacts around the globe<sup>1–3</sup>. It has two opposing phases (i.e., El Niño and La Niña), which are not simple mirror images and exhibit striking asymmetries in their dynamics, climate impacts, and predictability<sup>4–7</sup>. One of the most remarkable nonlinear characteristics of ENSO is its amplitude asymmetry (hereafter referred to as ENSO asymmetry for convenience), which describes the fact that sea surface temperature (SST) anomalies during strong El Niño episodes are more intense and farther east than during La Niña episodes. Consequently, the ENSO cycle has non-zero accumulation effects, influencing low-frequency variability as well as future projections of global climate<sup>8–11</sup>.

The ENSO asymmetry largely arises from nonlinear physical processes of strong-to-extreme ENSO events. For instance, early studies suggested that positive surface layer nonlinear dynamical heating (NDH) during extreme El Niño events is crucial for ENSO asymmetry<sup>12,13</sup>. The detailed roles of horizontal and vertical NDH components, however, were found to be sensitive to reanalysis products<sup>14</sup>. Others argued that strong positive NDH residing in the subsurface ocean owing to a disrupted equatorial undercurrent under extreme El Niño conditions also contributes to ENSO asymmetry by inhibiting the subsequent La Niña development in the eastern Pacific<sup>15</sup>. Aside from nonlinear ocean dynamics, asymmetric atmosphere–ocean coupling processes are also important<sup>16–18</sup>. Zonal wind stress anomalies are more intense

and farther east during the El Niño phase than during the La Niña phase, resulting in asymmetric SST growth rates by affecting the amplitude of the positive dynamic feedback<sup>19,20</sup>. In particular, the eastward shift of atmospheric convection can push El Niño to a larger amplitude through anomalous zonal advection of western Pacific warm water<sup>21</sup>. Also, the eastward expansion of the Pacific warm pool under extreme El Niño conditions markedly reduces meridional SST gradients in the eastern Pacific, moves the Intertropical Convergence Zone (ITCZ) equatorward<sup>22</sup>, and causes a huge nonlinearity in the atmospheric feedback<sup>23</sup> not observed in moderate El Niño cases. Such asymmetry and nonlinearity in the air–sea coupling are primarily attributed to the inherent nonlinear dependence of deep convection on SST<sup>24</sup>. Furthermore, nonlinear interactions between ENSO and high-frequency variability, such as state-dependent westerly wind bursts in the tropical western Pacific, oceanic instability waves in the tropical eastern Pacific, and sub-mesoscale oceanic eddies, as well as biophysical processes, all contribute to ENSO asymmetry<sup>25–30</sup>.

Despite remarkable progress in understanding ENSO nonlinear processes, most state-of-the-art climate models are still struggling to simulate ENSO asymmetry realistically<sup>11,31,32</sup>. This poor performance is possibly related to common model biases of the tropical Pacific mean state, such as an excessive westward extension of the cold tongue and stronger mean trade winds compared to observations, which tend to weaken the atmosphere–ocean interactions and hampers the occurrence of strong convective El Niño events<sup>31–37</sup>. Reliable future projections of ENSO characteristics in a changing climate, particularly strong ENSO events with

<sup>1</sup>Irreversible Climate Change Research Center, Yonsei University, Seodaemun-gu, Seoul 03722, Republic of Korea. <sup>2</sup>Department of Atmospheric Sciences, Yonsei University, Seodaemun-gu, Seoul 03722, Republic of Korea. <sup>3</sup>Division of Environmental Science and Engineering, Pohang University of Science and Technology (POSTECH), Pohang, Republic of Korea. <sup>4</sup>Department of Atmospheric Sciences, School of Ocean and Earth Science and Technology (SOEST), University of Hawai'i at Mānoa, Honolulu, HI 96822, USA. <sup>5</sup>Department of Oceanography & International Pacific Research Center (IPRC), School of Ocean and Earth Science and Technology (SOEST), University of Hawai'i at Mānoa, Honolulu, HI 96822, USA. <sup>6</sup>CIC-FEMD/ILCEC, Key Laboratory of Meteorological Disaster of Ministry of Education (KLME), Nanjing University of Information Science and Technology, Nanjing 210044, China. <sup>7</sup>School of Atmospheric Sciences, Nanjing University of Information Science and Technology, Nanjing 210044, China. <sup>8</sup>Institute for Convergence Research and Education in Advanced Technology, Yonsei University, Seoul, South Korea. <sup>9</sup>Key Laboratory of Transportation Meteorology, China Meteorological Administration (CMA), Nanjing 210041, China. <sup>10</sup>Jiangsu Meteorological Service Centre, Nanjing 210041, China. ✉email: [sian@yonsei.ac.kr](mailto:sian@yonsei.ac.kr)

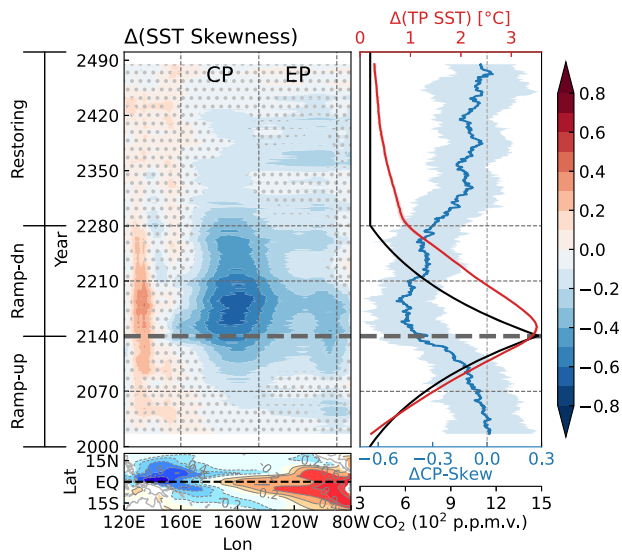


**Fig. 1 Hysteresis of SST skewness.** Ensemble-averaged SST anomaly skewness (unitless) in the equatorial (5°S–5°N) Pacific (Hovmöller plot, shading) and equatorial central Pacific (right plot, blue line) relative to the present-day control simulation (bottom map insert, shading, and contours). Non-stippled areas in the Hovmöller plot denote the skewness changes exceeding the 95% confidence level. The black and red solid lines in the right plot represent the CO<sub>2</sub> concentration and ensemble-averaged tropical Pacific SST (TP SST, 120°E–80°W, 20°S–20°N) change, respectively. The superimposed colored shadings represent two inter-member standard deviations spread of related physical quantities. Vertical dashed lines in the Hovmöller plots indicate the eastern (90°–145°W) and central Pacific (160°E–145°W) regions, respectively. Horizontal dashed lines indicate different stages of CO<sub>2</sub> forcing. The  $\Delta$  symbol indicates the ensemble-average change relative to the control simulation ensemble average.

devastating socioeconomic consequences and ENSO asymmetry thereof, are thus largely capped by these model deficiencies<sup>38–40</sup>. For example, one study showed that the intensification of upper ocean stratification in response to global warming enhances the ocean-atmosphere coupling, leading to increased SST variability and stronger El Niño events in the eastern Pacific<sup>41</sup>. However, an opposing viewpoint suggested that a stiffer thermocline suppresses nonlinear ocean responses to wind perturbations, which dampens strong El Niño events and thereby weakens ENSO asymmetry<sup>42</sup>. Ham<sup>43</sup> also provided multi-model ensemble evidence for a weakened ENSO asymmetry in response to global warming but mainly emphasized the role of altered SST-precipitation sensitivity. These results suggest that future changes in ENSO asymmetry and their possible causes are not fully understood yet<sup>44</sup>.

Aside from investigating projected changes under different future warming scenarios, there has also been a growing interest in exploring climatic responses to possible mitigation actions, like CO<sub>2</sub> removal<sup>45–50</sup>. This CO<sub>2</sub> removal scenario not only provides useful information on mitigation but also an altered perspective to unravel the details of potential ENSO asymmetry changes in response to global warming. It has been suggested that major climate elements, such as the Atlantic Meridional Overturning Circulation and the Intertropical Convergence Zone (ITCZ), exhibit prominent hysteresis responses when CO<sub>2</sub> is reduced<sup>51,52</sup>. While those background state changes could theoretically affect ENSO properties, the response of ENSO asymmetry to such a CO<sub>2</sub> perturbation has not been investigated. For our investigation, we conducted large ensemble simulations using a climate model with authentic representations of ENSO nonlinear features and an idealized specified CO<sub>2</sub> ramp-up and ramp-down pathway.

Through comparisons between different CO<sub>2</sub> stages (i.e., ramp-up and ramp-down), we aim to deepen the current understanding of ENSO characteristics changes and their underlying physical processes relating to tropical Pacific background states in the context of climate change, particularly for strong-to-extreme ENSO regimes.

## RESULTS

### Hysteresis of equatorial SST skewness

Following previous studies<sup>4,11,53</sup>, we used the statistical metric of skewness (Methods) to quantify the ENSO asymmetry. In the present-day (PD) control simulation (Methods), the tropical Pacific SST skewness shows a zonal dipole structure (Fig. 1) resembling the satellite era observations (Supplementary Fig. 1), albeit with an underestimated magnitude in the eastern Pacific and an overall slightly westward-extended pattern, suggesting a generally realistic representation of ENSO's nonlinear characteristics by this generation of the model release<sup>54–56</sup>. To investigate how the ENSO asymmetry responds to CO<sub>2</sub> forcing changes, we calculated the skewness of monthly SST anomalies over a 31-year moving window, subsequently averaged over all 28 ensemble members, and expressed the results relative to the PD simulation (Fig. 1). During the ramp-up period of CO<sub>2</sub> concentrations (i.e., years 2001–2140), we observe moderate changes in SST skewness, with positive and negative skewness located to the west and east of 160°E, respectively. These changes counteract the mean state of skewness in the PD simulation and indicate an overall reduction of equatorial Pacific SST asymmetry. As CO<sub>2</sub> concentrations approach their peak phase (i.e., 1468 p.p.m.v.), the forced negative skewness responses over the central-to-eastern Pacific become significant at the 95% confidence level, consistent with one previous finding of a weakened ENSO SST asymmetry under global warming<sup>43</sup>.

Interestingly, the skewness changes are even more pronounced during the ramp-down period (i.e., years 2141–2280), suggesting a possibility of hysteresis in ENSO asymmetry. Specifically, the negative skewness change in the central Pacific (location of the near-zero skewness in the PD simulation) reaches a minimum value of about  $-0.6$  around the year 2180, before gradually recovering over the next centuries. In contrast to the largely uncertain response during the ramp-up period, the negative change during the ramp-down period is significantly distinguishable from zero at the 95% confidence level. Such a persistent change cannot be explained by thermodynamic processes alone, as evidenced by its distinct time scale compared to the thermal inertia-induced hysteresis changes in the tropical Pacific background SST, which closely follows the CO<sub>2</sub> forcing trajectory during the ramp-up period and lags slightly behind the CO<sub>2</sub> forcing by  $\sim 10$  years during the ramp-down period (Fig. 1). The skewness decrease in the eastern Pacific (90°–145°W) is comparatively weaker, but still significant at the 95% confidence level, with apparent signals mostly concentrated in the first half of the ramp-down period (i.e., years 2141–2210, ramp-down-I). The skewness change in the western Pacific also peaks during the ramp-down-I period and shows a similar temporal evolution to that in the central Pacific, albeit with a reversed sign and a much narrower zonal extent of only  $\sim 10^\circ$  longitude. These regionally dependent responses of ENSO asymmetry suggest different underlying physical mechanisms. When the CO<sub>2</sub> concentration was further restored to its PD level (i.e., years 2281–2500; 367 p.p.m.v.), the skewness changes slowly converge to zero toward the end of the simulation, showing a reversible response on timescales of a few centuries, but beyond human perceptible timescales.

### Skewness decomposition and ENSO asymmetry

The SST skewness in the tropical Pacific represents the asymmetry part between El Niño and La Niña phases. Therefore, we presented

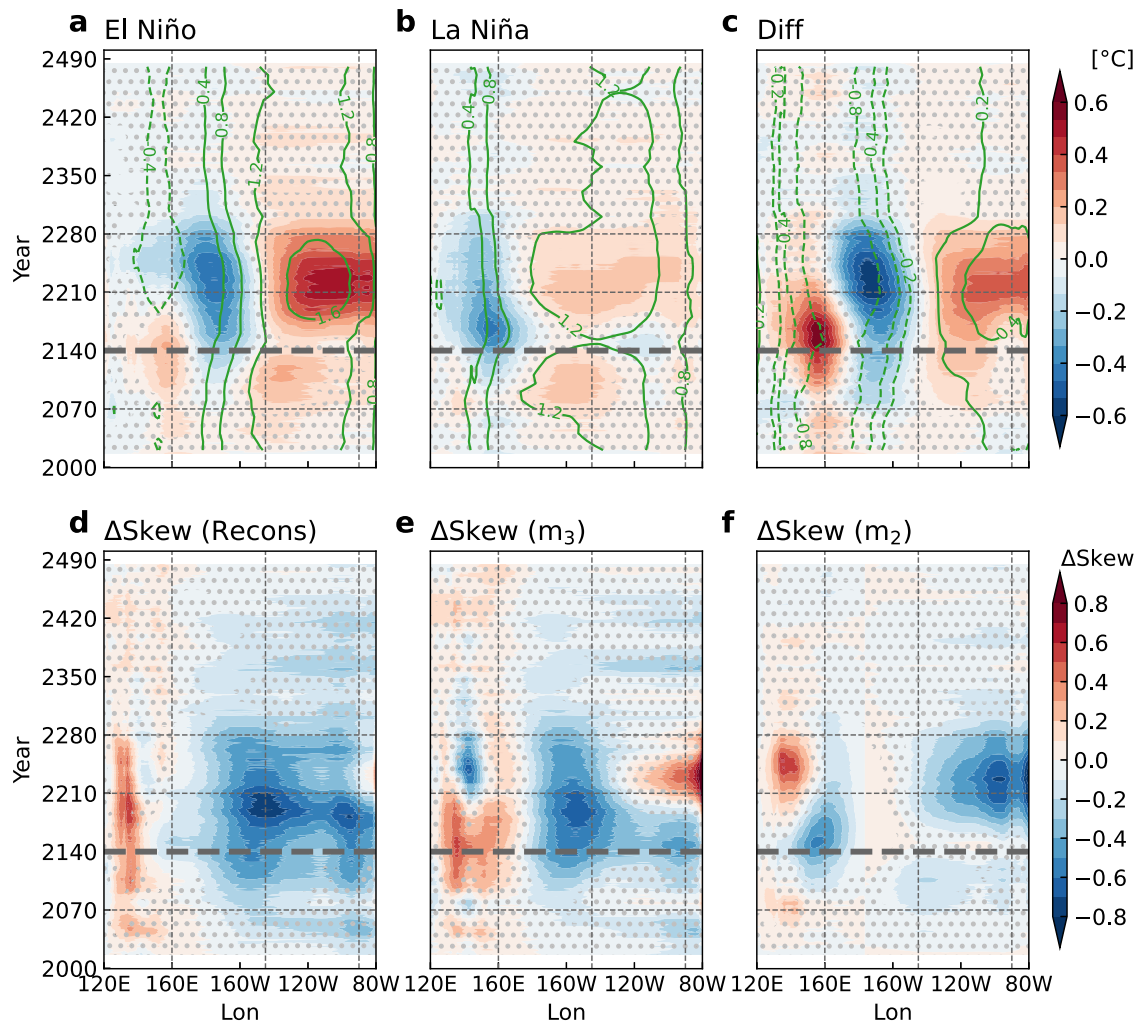


**Fig. 2 ENSO SST asymmetric changes and skewness decomposition.** **a–c** Ensemble-averaged Hovmöller diagrams of equatorial (5°S–5°N) Pacific SST anomalies (contours, unit: °C) regressed onto standardized central-to-eastern Pacific (90°–180°W, 5°S–5°N) ENSO SST index and their changes relative to the control simulation (shading, unit: °C) under the **(a)** El Niño phase, **(b)** La Niña phase, and **(c)** El Niño–La Niña difference. **d** Ensemble-averaged Hovmöller diagrams of equatorial (5°S–5°N) Pacific reconstructed skewness changes, **(e)** contributions by the third-moment changes ( $m_3$ ), and **(f)** second-moment changes ( $m_2$ ). Vertical dashed lines in each Hovmöller plot indicate the eastern (90°–145°W) and central Pacific (160°E–145°W) regions, respectively. Horizontal dashed lines indicate different stages of CO<sub>2</sub> forcing. The  $\Delta$  symbol indicates the ensemble-average change relative to the control simulation ensemble average. Non-stippled areas in each plot denote corresponding physical quantity changes exceeding the 95% confidence level.

the evolving SST patterns for both El Niño and La Niña phases, as well as their changes relative to the PD simulation, to elucidate their respective contributions to the skewness changes (Fig. 2a, b). Here, ENSO patterns were derived by separately regressing SST anomalies onto the positive and negative phases of the central-to-eastern equatorial Pacific (90°–180°W, 5°S–5°N) SST index that mainly encompasses the ENSO’s action center (Methods). As such, both El Niño SST and La Niña SST have positive signs with positive changes representing intensification and negative changes representing a reduction. Compared to the ramp-up period, the El Niño SST anomaly becomes stronger (~0.5 °C) and more eastward during the ramp-down period, exhibiting a clear hysteresis feature (Fig. 2a). In particular, the accompanied eastward shift of the El Niño SST western edge greatly reduces the central Pacific SST magnitude.

La Niña SST changes are roughly similar to those of El Niño but with a smaller amplitude (~0.15 °C) and a westward zonal shift of its centroid by about 25° longitude (Fig. 2b). Specifically, the La Niña SST in the eastern Pacific becomes significantly stronger at the 95% confidence level around the middle of the ramp-down

period, coinciding with a simultaneous increase in eastern Pacific El Niño intensity. A similar eastward shift of La Niña’s western edge also occurs during the ramp-down phase, leading to negative changes in western Pacific SST that are not observed during the ramp-up period. Intriguingly, the La Niña SST changes in the central Pacific are generally symmetric with regard to the CO<sub>2</sub> forcing and thus show a weak hysteresis feature. Here, the asymmetric response of El Niño and La Niña SST to CO<sub>2</sub> forcing may arise from their inherent asymmetric air–sea coupling dynamics. In particular, El Niño-related precipitation anomalies in the central-eastern Pacific continuously intensify and move eastward until the middle of the ramp-down phase (the year 2210), inducing similar hysteresis changes in zonal surface wind stress anomalies (Supplementary Fig. 2a) and thus further favoring positive SST anomaly increases during the ramp-down period. In contrast, La Niña-related atmospheric responses are mainly confined to the central-to-western Pacific, with weaker magnitude and less hysteresis feature (Supplementary Fig. 2b), less effective for La Niña SST growth when CO<sub>2</sub> is reduced. The overall weak La Niña SST changes imply a dominant role of the El Niño phase in

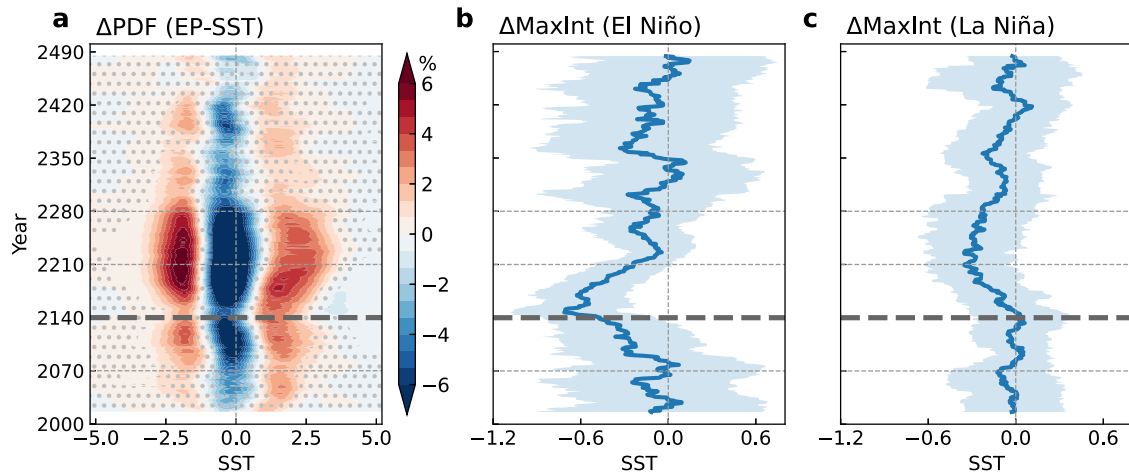


**Fig. 3** Changes in eastern Pacific SST probability density function (PDF) and ENSO maximum intensity. **a** Ensemble-averaged PDF changes (shading, unit: %) of eastern Pacific (90°–145°W, 5°S–5°N) SST anomalies relative to the present-day control simulation. Time evolution of November–December–January (NDJ) averaged SST maximum intensity in **(b)** the El Niño phase and **(c)** the La Niña phase. The vertical dashed line in each plot indicates SST anomalies with zero value while horizontal dashed lines indicate different stages of CO<sub>2</sub> forcing. The  $\Delta$  symbol indicates the ensemble-average change relative to the control simulation ensemble average. Non-stippled areas in **(a)** denote SST PDF changes exceeding the 95% confidence level.

the central-to-eastern Pacific ENSO SST asymmetry changes, as is evidenced by their similar evolution patterns (Fig. 2a,c). In particular, the hysteresis of the central Pacific skewness decrease (Fig. 1) is primarily due to a more compact horizontal structure of El Niño SST during the ramp-down period (Fig. 2a). However, the skewness changes in the eastern Pacific (Fig. 1) cannot be readily explained by linear SST differences (Fig. 2c) and involve other factors as will be shown below.

By definition, the skewness is a normalized metric with the third statistical moment ( $m_3$ ) scaled by the standard deviation cubed. Thus, the temporal variations of skewness may be implicitly driven by ENSO variance changes. Considering this, we introduced a linear decomposition approach (“Methods” section) to separate the contributions of the  $m_3$  and the second statistical moment (i.e., variance,  $m_2$ ). As shown, the skewness changes can be largely reconstructed despite slight shifts in the pattern center (Figs. 1 and 2d), possibly due to the nonlinear nature of the skewness metric and/or an imperfect independent relationship between  $m_3$  and  $m_2$ . The contribution of the  $m_3$  changes (Fig. 2e) physically represents changes in SST amplitude difference between El Niño and La Niña phases (Fig. 2c), as evidenced by their similar pattern. In particular, the hysteresis feature of central Pacific negative skewness changes (Fig. 1) is predominantly contributed by El Niño-related  $m_3$  changes (Fig. 2e and Supplementary Fig. 3a), consistent with a key role of the El Niño pattern eastward displacement (Fig. 2a) as discussed before.

However, the negative skewness in the eastern Pacific responses is more complicated, involving contributions from changes in both the  $m_2$  and  $m_3$  (Fig. 2e, f). During the ramp-down-I period (i.e., years 2141–2210), a negative contribution from  $m_3$  (Fig. 2e) suggests that the local skewness changes are partly contributed by ENSO amplitude asymmetry. Further separation reveals joint contributions from both ENSO phases (Supplementary Fig. 3). In particular, the El Niño-induced negative  $m_3$  changes (Supplementary Fig. 3a) contribute to the skewness change in the first 2–3 decades after the CO<sub>2</sub> peak, while the La Niña-induced negative  $m_3$  changes (Supplementary Fig. 3b) are more important around the middle of the ramp-down period (the year 2210). Since  $m_3$  is particularly sensitive to extreme values, the different peak timing of  $m_3$  contributions between the two ENSO phases implies distinct changes in extreme ENSO events. To test this hypothesis, we further examined changes in the probability density function (PDF) of the eastern Pacific SST anomalies (Fig. 3a). It shows that

the SST anomaly PDF generally exhibits a flattening response to CO<sub>2</sub> forcing, with the probability of SST anomalies around neutral states decreasing while the probability of those on both sides increases, suggesting increased ENSO SST variability in the eastern Pacific. Interestingly, around the CO<sub>2</sub> peak phase on the El Niño side, the SST anomaly PDF shows significantly negative changes between 2.5–5.0 °C (Fig. 3a), which extrudes the overall increasing tendency of the warm SST anomaly probability and indicates an opposite decreasing behavior of the extreme El Niño occurrence. Similar divergent responses are not found for the La Niña phase. The La Niña-related probability increases consistently for negative SST anomalies of different intensities and reaches a maximum around the year 2210. Accordingly, the maximum intensity of the eastern Pacific SST anomalies, another indicator of ENSO amplitude asymmetry<sup>4,12</sup>, decreases by about 0.6 °C for the El Niño phase shortly after the CO<sub>2</sub> peak (Fig. 3b) while is slightly enhanced by  $\sim -0.3$  °C for the La Niña phase (Fig. 3c) around the middle of the ramp-down period. The divergent and temporal dislocation of extreme El Niño and extreme La Niña responses explain the contribution of ENSO amplitude asymmetry to eastern Pacific negative skewness changes during the ramp-down-I period (Fig. 2e), which cannot be readily understood by asymmetric SST differences from a linear perspective (Fig. 2c).

During the ramp-down-II period (years 2211–2280), the relatively weak eastern Pacific skewness decrease (Fig. 1) is a residual result stemming from cancellations between the enhanced eastern Pacific ENSO amplitude asymmetry (i.e., positive  $m_3$  contribution; Fig. 2c, e) and a negative scaling effect from locally enhanced SST variability (i.e., negative  $m_2$  contribution; Fig. 2f). Owing to the increased strong El Niño variability and the recovery of El Niño’s maximum intensity (Fig. 3a, b), the contribution of  $m_3$  reverses its negative sign to positive after the year 2210 (Fig. 2e), implying an increased absolute ENSO SST amplitude asymmetry compared to the PD simulation. In contrast, stronger ENSO variability naturally has a negative scaling effect (Fig. 2f) by increasing the denominator of the skewness metric. The disproportionate changes in  $m_3$  and  $m_2$  can be physically interpreted as a higher frequency of regular strong ENSO cycles, which increases the overall ENSO variability but reduces the proportion of extreme El Niño events that elevates skewness values accordingly. Here, the modestly increased La Niña intensity as part of the stronger ENSO cycle mainly results from enhanced El Niño-induced ocean discharge processes, as evidenced by the

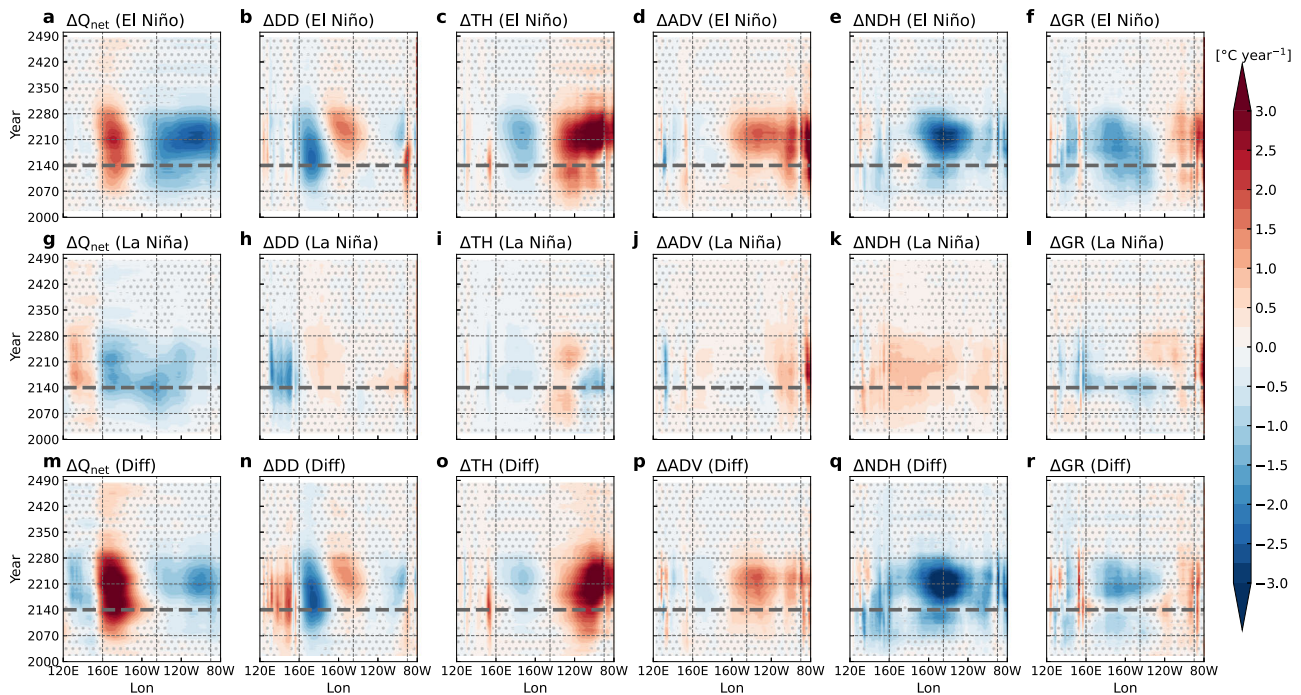


**Fig. 4** Asymmetric changes in ENSO feedback strengths. **a–f** Hovmöller diagrams of changes in ensemble-averaged equatorial ( $5^{\circ}\text{S}$ – $5^{\circ}\text{N}$ ) Pacific regressed feedback strengths (unit:  $^{\circ}\text{C year}^{-1}$ ) on the simultaneous positive phase (El Niño) of normalized monthly ENSO SST anomaly index ( $180^{\circ}$ – $90^{\circ}\text{W}$ ,  $5^{\circ}\text{S}$ – $5^{\circ}\text{N}$ ) using a 31-year moving window. **g–l** as **a–f**, but for the negative phase (La Niña) of the normalized ENSO SST anomaly index. **m–r** show differences between the El Niño and La Niña phases.  $Q_{\text{net}}$ , DD, TH, ADV, NDH, and GR represent surface net heat flux, dynamical damping, thermocline feedback, advective feedback, nonlinear dynamical heating, and net growth rate of SST anomalies, respectively. Detailed formula expressions for each feedback symbol and calculation procedures are available in the Methods section. Vertical dashed lines denote the eastern and central Pacific while horizontal dashed lines indicate different stages of  $\text{CO}_2$  forcing. The  $\Delta$  symbol indicates the ensemble-average change relative to the control simulation ensemble average. Non-stippled areas in each plot denote feedback changes exceeding the 95% confidence level.

stronger interannual alignment of warm-to-cold ENSO events and the associated more pronounced shoaling of the equatorial Pacific zonal mean thermocline in the transition phase (Supplementary Fig. 4), and its role in skewness reduction has been implicitly accounted for by increasing the  $m_2$  (Fig. 2f) and limiting the  $m_3$  changes (Fig. 2e and Supplementary Fig. 3b), respectively. We also note that although the ensemble-averaged maximum El Niño intensity recovers quickly, it is still lower than in the PD control simulation during the ramp-down-II period (Fig. 3b). This places a limit on the potential increase in the extreme El Niño magnitude despite the concurrent increase in El Niño activity, further highlighting the scaling effects of the intensified ENSO cycle.

Similar statistical scaling effects also occur in the eastern Pacific during the ramp-up and ramp-down-I period, as well as in the western Pacific region (Fig. 2f). In other words, ENSO SST skewness and its future changes, depending on the entire shape of the SST anomaly PDF, are influenced not only by changes in the linear asymmetry of SST intensity between ENSO phases (i.e., in the central Pacific) but also by the relative frequency of ENSO events with different intensities, particularly extreme cases (i.e., in the eastern Pacific). Considering the western Pacific skewness change involves a more complex nature with several small-scale features in both the  $m_2$  and  $m_3$  contributions (Fig. 2e, f), we will primarily focus on the ENSO core region of the central-to-eastern equatorial Pacific in our subsequent analysis.

#### Changes in air-sea coupling processes and feedback strength

From a linear perspective, both the central Pacific El Niño SST decrease and the eastern Pacific El Niño SST increase are largely related to an intensification and eastward shift of El Niño's action center (Fig. 2a and Supplementary Fig. 2a), despite their

contrasting roles in local negative skewness changes. In this section, we analyzed the detailed feedback processes relative to the PD control simulation (Supplementary Fig. 5) to understand linear SST changes and skewness hysteresis using an ocean mixed-layer heat budget analysis ("Methods" section). The physical mechanisms associated with extreme El Niño changes are discussed in the next section. As shown, the feedback terms show larger changes and more pronounced hysteresis features in the El Niño phase than in the La Niña phase, with the former dominating their difference (Fig. 4), possibly due to their asymmetric sensitivity of atmospheric responses (Supplementary Fig. 2) as discussed earlier. Here, we note that the feedback changes are consistent with our previous analysis of ENSO SST, both defined in an asymmetric regression framework ("Methods" section) and thus different from the usual composite analysis in sign.

In the central Pacific, the changes in the El Niño ocean dynamical damping (DD; Fig. 4b and Supplementary Fig. 5b) and nonlinear dynamical heating (NDH; Fig. 4e and Supplementary Fig. 5e) terms play a dominant role in decreasing the local SST anomalies during the ramp-down period and contribute most to the SST asymmetry changes in the western and eastern regions, respectively (Fig. 4n, q). Both feedback changes dominated by their zonal component (Supplementary Fig. 6a–e) reflect a zonal eastward shift of their counterparts in the PD simulation (Supplementary Fig. 5b,e), mainly through the interactive coupling with a simultaneous eastward shift of the El Niño SST center (Fig. 2a). More specifically, the eastward retreat of the El Niño SST western edge causes an increase in the anomalous zonal SST gradient near  $160^{\circ}\text{W}$  and a decrease near  $160^{\circ}\text{E}$ , creating a zonal dipole change of central Pacific SST zonal gradient (Supplementary Fig. 7a). These SST anomaly zonal gradient changes can work

with the background ocean zonal current changes (Supplementary Fig. 7e) to produce a similar structural change in the DD feedback (Fig. 4b) and nonlinearly interact with El Niño zonal current changes (Supplementary Fig. 7c) to generate a central Pacific nonlinear dynamical cooling (Fig. 4e). Meanwhile, the reduction of the central Pacific El Niño SST weakens the local thermal damping feedback ( $Q_{\text{net}}$ ; Supplementary Fig. 5a), with a positive change (Fig. 4a) dominated by the shortwave component (Supplementary Fig. 6f–i), which in turn counteracts the local SST decrease. Changes in thermocline feedback (TH) and advective feedback (ADV) are comparatively small and thus less important in the central Pacific (Fig. 4c, d and Supplementary Fig. 5c, d). The combined effects of these competing feedbacks reduce the net growth rate (GR) of the central Pacific SST anomalies (Fig. 4f and Supplementary Fig. 5f), reducing the El Niño SST magnitude and contributing to the local negative skewness changes.

In the eastern Pacific, during the ramp-down period, the increased SST activity is mainly attributed to the enhanced TH feedback and ADV feedback (Fig. 4c, d and Supplementary Fig. 5c, d), which are two leading positive feedbacks of ENSO events<sup>57</sup>. In particular, the El Niño center continuously intensifies and moves eastward until about the middle of the ramp-down period (i.e., the year 2210), showing pronounced hysteresis behavior (Fig. 2a and Supplementary Fig. 2a). The anomalous zonal surface wind stress responses also strengthen and shift eastward (Supplementary Figs. 2a and 7b), leading to stronger thermocline responses in the eastern Pacific and driving larger eastward zonal surface current anomalies (Supplementary Fig. 7c, d) by increasing the zonal mean momentum flux input and enhancing the coupling sensitivities between zonal wind stress and the eastern Pacific thermocline depth as well as the associated zonal current<sup>58</sup>. These changes favor the above two positive feedbacks and local SST anomaly growth. Meanwhile, as El Niño eastern Pacific SST becomes stronger during the ramp-down period, the local damping effect of  $Q_{\text{net}}$  (Supplementary Fig. 5a) also becomes enhanced, with a negative change (Fig. 4a) dominated by latent heat flux and shortwave radiation (Supplementary Fig. 6f–i). The change in NDH (Fig. 4e and Supplementary Fig. 5e) plays a slightly damping role in the western part of the eastern Pacific (~145°W), while the changes in the DD term (Fig. 4b and Supplementary Fig. 5b) are overall negligible in the eastern Pacific. All these changes in feedback strength produce a positive net GR of the eastern Pacific SST anomalies (Fig. 4f), which increases the magnitude of the concurrent El Niño SST and further leads to a stronger subsequent La Niña in the eastern Pacific with excessive ocean discharge processes as discussed before. The resulting higher ENSO variability reduces the skewness via the statistical scaling effect.

La Niña changes also have non-negligible contributions to the decrease in eastern Pacific skewness. However, its changes almost passively follow the increased El Niño activity in the eastern Pacific and exhibit much weaker changes in feedback strength. During the ramp-down-II period, the moderate increase in the eastern Pacific La Niña intensity is consistent with a simultaneous increase in net SST growth rate (Fig. 4l and Supplementary Fig. 5l), as dominated by the enhanced thermocline feedback (Fig. 4i and Supplementary Fig. 5i) owing to the El Niño-induced excessive discharge of equatorial oceanic heat content (Supplementary Fig. 4). Changes in the advective feedback and nonlinear feedback also play some positive roles but are of secondary importance (Fig. 4j, k and Supplementary Fig. 5j, k). Similar results became more apparent by casting feedback into the ENSO's seasonal evolution cycle (Supplementary Fig. 8). The critical role of the thermocline feedback in the ENSO phase transition and subsequent La Niña growth is consistent with Jin's recharge oscillator theory<sup>59,60</sup> and observational diagnostic results<sup>20</sup>. Considering that La Niña shows an increased probability of negative SST anomalies with different intensity levels during ramp-down-II

(Fig. 3a), the linear feedback changes can also help explain the slightly increased eastern Pacific La Niña maximum intensity (Fig. 3c). We also noted the following interesting phenomenon: Although the central Pacific La Niña SST has a minor influence on the local skewness decrease with almost symmetrical increases with respect to the CO<sub>2</sub> forcing pathway (Fig. 2b), the local net growth rate changes of the SST are almost insignificant at the 95% confidence level, and even decrease around the CO<sub>2</sub> peak phase (Fig. 4l), mainly due to the enhanced damping effect changes contributed by the cloud-shortwave feedback (Supplementary Fig. 9). In this case, the slightly increased La Niña intensity may be solely due to a reduced baseline level of warm SST anomalies from the precedent El Niño phase<sup>61</sup>, as the La Niña typically follows El Niño.

### Effects of ITCZ hysteresis and El Niño-like background warming

The hysteresis of equatorial air-sea coupled processes and their reflection in individual feedback strength changes are influenced by tropical Pacific background climate state change. First, the changes in El Niño feedbacks and related state variables over the central-to-eastern equatorial Pacific region, such as SST (Fig. 2a), precipitation (Supplementary Fig. 2a), surface zonal current anomalies (Supplementary Fig. 7c), and thermocline depth anomalies (Supplementary Fig. 7d), all reach a peak around the middle of the ramp-down period (i.e., 2210). Such a long time lag compared to the CO<sub>2</sub> peak phase (~70 years) cannot be solely attributed to the thermal inertia of the equatorial ocean. For example, an El Niño-like background SST warming in the equatorial eastern Pacific has been proposed to thermodynamically enhance the ENSO atmospheric responses and the resulting air-sea coupling strength<sup>62,63</sup> by increasing the availability of the background moisture through the Clausius-Clapeyron constraint relation<sup>64</sup>. However, it peaks only around the year 2160 (Fig. 5d) and is not consistent with the observed long-time lag of ENSO coupling changes.

Interestingly, we noted that the meridional position of the tropical Pacific ITCZ (Fig. 5a) shares a similar hysteresis timescale with the equatorial air-sea coupling strength, suggesting their potential physical linkages. Compared to the ramp-up period, the ITCZ moves closer to the equator accompanied by a more eastward extension of the South Pacific Convergence Zone during the ramp-down period (Fig. 5b, c). A related study suggests that the ITCZ hysteresis is primarily driven by an interhemispheric energy imbalance<sup>52</sup> due to the slow recovery of the Atlantic Meridional Overturning Circulation<sup>51</sup> and the larger heat capacity of the Southern Ocean<sup>65</sup>. Based on our previous results<sup>58</sup>, such a near-symmetric structure of tropical Pacific background rainfall with respect to the equator can facilitate the development of off-equatorial atmospheric disturbances during the early stage of El Niño, which in turn favors the occurrence of El Niño, intensifies the equatorial air-sea coupling strength, and displaces the coupling center eastward. Since our focus in this study is on projected changes in ENSO skewness, we refer the reader to the above studies for the details on ITCZ hysteresis and the physical links between ITCZ and El Niño variability.

It is worth noting that the negative change in eastern Pacific skewness during the ramp-down-I period (i.e., years 2141–2210) is due to the large reduction in extreme El Niño events (Fig. 3a and Supplementary Fig. 3a), which cannot be explained by coupling strength changes from a linear perspective. Early studies suggested that the maximum potential intensity of El Niño is physically constrained by zonal SST differences between the warm pool and the cold tongue<sup>4,12</sup>. Recent studies also provide similar evidence based on future climate change scenario experiments of Earth system models<sup>39,40,66</sup>. The general underlying mechanism is that the cold tongue SST cannot exceed the radiative-convective equilibrium temperature of the climatological warm pool, even

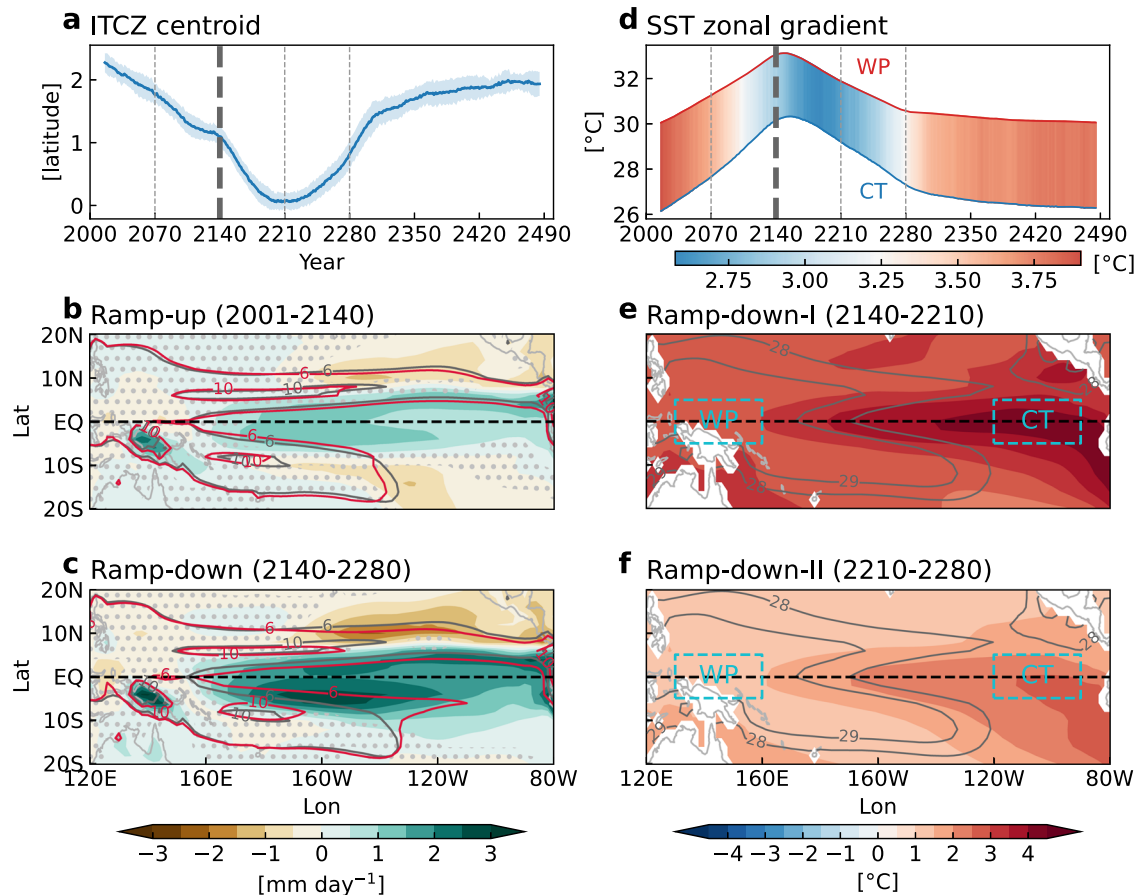


**Fig. 5** Changes in tropical Pacific background states. **a** Time evolution of ensemble-averaged tropical Pacific (120°E–80°W, 20°S–20°N) precipitation centroid (unit: degrees latitude). The blue shading represents two inter-member standard deviations spread. Ensemble-averaged precipitation (unit: mm day<sup>-1</sup>, red contours) and corresponding changes relative to the control simulation (shading) during the **(b)** ramp-up period and the **(c)** ramp-down period. Gray contours represent long-term mean precipitation in the control simulation. **d** Time evolutions of ensemble-averaged SST indices (unit: °C) in the warm pool (130–160°E, 5°S–5°N; red line), cold tongue (90–120°W, 5°S–5°N; blue line), and their differences (shading). Ensemble-averaged SST relative to the control simulation (shading) during the **(e)** first half of the ramp-down period (ramp-down-I), and the **(f)** second half of the ramp-down period (ramp-down-II). Gray contours represent long-term mean SST in the control simulation. Non-stippled areas in each map denote related physical quantity changes exceeding the 95% confidence level.

when the warm pool expands far to the east and occupies the climatological cold tongue under extreme El Niño conditions. In our study, owing to the thermal inertia of the tropical ocean, the response of the El Niño-like background state reaches a maximum of about 2–3 decades after the CO<sub>2</sub> peak (Fig. 5d–f). Correspondingly, the zonal contrast of the equatorial Pacific SST mean state becomes more diminished during the ramp-down-I period than in other periods (Fig. 5d–f). This strongly reduces the upper limit and occurrence probability of extreme El Niño events and thus contributes to the simultaneous SST skewness decrease in the eastern Pacific.

The above results also indicate that the long hysteresis timescale of the ENSO SST asymmetry, or ENSO properties in a general sense, is largely determined by the time lag of the tropical Pacific climate background state to CO<sub>2</sub> removal, which is further suggested to be proportional to the peak CO<sub>2</sub> concentration<sup>49</sup>. In our experimental design, the CO<sub>2</sub> forcing has a long ramp-up period of 140 years and a high peak level (i.e., 1468 p.p.m.v.), which may exaggerate the timescale of ENSO SST asymmetry hysteresis. Therefore, we could in reality experience a shorter time lag of ENSO statistics hysteresis as long as CO<sub>2</sub> declines from a lower peak, for example, under the mitigation target set by the Paris Agreement. Given the high relevance of this issue for mitigation policy, more studies with different CO<sub>2</sub> pathways are

needed to gain a deeper understanding and accurate assessment of benefits and costs.

## DISCUSSIONS

In this study, we investigated the projected ENSO skewness changes and possible causes using an idealized CO<sub>2</sub> removal ensemble simulation with the CESM1.2 model. It was found that ENSO skewness change exhibits a pronounced hysteresis under this CO<sub>2</sub> pathway. An initially moderate reduction in ENSO skewness during the ramp-up period over the central-to-eastern equatorial Pacific becomes much more pronounced as CO<sub>2</sub> begins to decline after its peak level (i.e., 1468 p.p.m.v.). The central Pacific experiences the most pronounced hysteretic response, primarily due to an eastward displacement of the El Niño SST anomaly center and the resulting changes in ENSO linear amplitude asymmetry during the ramp-down period. The comparatively moderate changes over the eastern Pacific are due to two competing factors. First, during the first half of the ramp-down period, the El Niño maximum intensity declines sharply in response to strong El Niño-like changes in the background state, thus contributing to the decrease in skewness. Second, due to a nearly symmetric interhemispheric ITCZ structure around the middle of the ramp-down period, the overall ENSO SST variability in the eastern Pacific increases, and the resulting statistical scaling

effect compensates for the ENSO amplitude asymmetry changes, leading to a weak skewness decrease. Here, the so-called statistical scaling effect of ENSO variability is a physical consequence of more strong warm-to-cold ENSO cycles and a resulting reduction in extreme El Niño events.

In addition to the physical processes in the ocean surface mixed layer, we here also examined subsurface factors such as subsurface NDH (Supplementary Fig. 10) and equatorial ocean stratification (Supplementary Fig. 11) to investigate their possible role. Consistent with previous finding<sup>15</sup>, there is a positive subsurface NDH signal beneath the central Pacific surface layer (100–200 m) during the El Niño phase in the PD simulation, which is dominated by its zonal component related to the weakened equatorial undercurrent (Supplementary Fig. 10a–d). The subsurface NDH signal favoring positive skewness in the eastern Pacific weakens around the CO<sub>2</sub> peak phase (Supplementary Fig. 10e, f), coinciding with a reduction in extreme El Niño events (Fig. 3a). In this context, the subsurface NDH can be considered as a possible reason for the reduced skewness during the quiescent period of extreme El Niño activity. Following an increase in ENSO variability around the middle of the ramp-down period, the subsurface NDH also increases along with its positive contribution to skewness (Supplementary Fig. 10e, f), but this is largely offset by the scaling effects of changes in ENSO variability (Fig. 2f). In contrast, in the presence of the El Niño-like background state changes, upper ocean stratification increases in both the central and eastern Pacific (Supplementary Fig. 11). The maximum stratification change coincides with a reduction in extreme El Niño events and may therefore explain the concomitant decrease in eastern Pacific skewness<sup>42</sup>. However, such an increase in stratification may also enhance the oceanic response to wind forcing and contribute to the overall increase in ENSO variability in other periods<sup>41</sup>. Therefore, the effect of monotonic changes in ocean stratification on non-monotonic changes in ENSO properties, if any, should be nonlinear, which may involve either a threshold for its reversal role or divergent mechanisms that depend on specific ENSO regimes. The detailed dynamics of extreme El Niño changes in response to greenhouse warming and their potential link to upper ocean stratification in this simulation will be investigated in our future studies.

## METHODS

### Model configuration, experimental design, and datasets

In our study, we utilized the fully coupled Community Earth System Model version 1.2 (CESM1.2)<sup>67</sup> to explore forced responses of ENSO skewness to CO<sub>2</sub> forcing. This model is composed of the atmosphere (Community Atmospheric Model version 5, CAM5), ocean (Parallel Ocean Program version 2, POP2), sea-ice (Community Ice Code version 4, CICE4), and land models (Community Land Model version 4, CLM4). The atmospheric and land components are configured with about 1° horizontal resolution and 30 vertical hybrid layers. The ocean model has 60 vertical levels, with a longitudinal resolution of 1° and a latitudinal resolution of ~0.33° near the equator that gradually increases to 0.5° near the poles.

We designed and conducted two experiments, that is, a present-day (PD) reference experiment and a perturbation experiment with a specified CO<sub>2</sub> ramp-up and ramp-down pathway. The PD experiment is integrated for 900 years with a fixed CO<sub>2</sub> concentration level (1×CO<sub>2</sub>, 367 p.p.m.v.) in the present climate. The CO<sub>2</sub> ramp-up and ramp-down experiment is branched from the PD experiment at different phases of the Pacific Decadal Oscillation and the Atlantic Multidecadal Oscillation to generate a total of 28 ensemble members. Each member is driven by identical time-varying CO<sub>2</sub> forcing for 500 years (Fig. 1), comprising a 1% year<sup>-1</sup> increase in CO<sub>2</sub> concentration for 140 years until the concentration is quadrupled (4×CO<sub>2</sub>, 1,468 p.p.m.v.,

ramp-up period), a subsequent symmetric 1% year<sup>-1</sup> decrease in CO<sub>2</sub> concentration for another 140 years until it returns to the initial level (1×CO<sub>2</sub>, 367 p.p.m.v., ramp-down period), and fixed CO<sub>2</sub> concentration for the remaining 220 years (1×CO<sub>2</sub>, 367 p.p.m.v., restoring period).

We also used the SST reanalysis dataset from the Extended Reconstructed Sea Surface Temperature, version 5 (ERSSTv5)<sup>68</sup> to examine the observational ENSO skewness. The analysis period was from 1979–2020 to ensure high data quality.

### Definition of diagnostic variables and indices

1. The thermocline depth is computed as the depth of the maximum vertical temperature gradient in the equatorial Pacific upper ocean (down to 350 m depth) for each grid cell and each ensemble member.

2. The precipitation centroid is defined as the latitude that splits the annual tropical Pacific (120°E–80°W, 20°S–20°N) zonal mean precipitation equally in half<sup>52,69</sup>. The precipitation is interpolated to a finer grid with a 0.1° increment in the meridional direction to accurately resolve the precipitation centroid.

### Definition of anomalies and significance test

All model variables were linearly interpolated onto a common grid with a 2°×2° horizontal spatial resolution and a 10 m vertical resolution in the upper ocean (down to 350 m depth). For the PD experiment, the climatology and anomalies are defined using the whole period of simulation. For the CO<sub>2</sub> perturbation experiment, the externally forced responses and anomalies of internal variability are calculated as the ensemble mean and related deviations in each member, respectively. Here, we note that the 28-member ensemble mean on a monthly timescale can largely reduce the internal variability and produce highly consistent ENSO anomalies and related hysteresis statistics compared to those using an additional 31-year moving average operator to define a smoother forced background state (not shown). For reanalysis data, SST anomalies were calculated relative to the seasonal climatology of the entire period (i.e., 1979–2020) and linearly detrend.

The statistical significances of 28-member ensemble-averaged results relative to the PD simulation were determined based on the two-tailed Student's *t*-test. In cases of analyses with a moving window (see below), the effective sample size of related quantity in the PD simulation equals the number of non-overlapping windows. For example, a 31-year moving window in the 900-year control simulation yields an effective sample size of 29.

### ENSO skewness definition and decomposition

ENSO asymmetry is measured by the statistical metric of anomalous SST skewness ( $\gamma$ ):

$$\left\{ \begin{array}{l} \gamma = \frac{m_3}{m_2^{3/2}} \\ m_k = \frac{1}{N} \sum_{i=1}^N (SST'_i)^k \quad (k = 2, 3) \end{array} \right. \quad (1)$$

The  $SST'_i$  and  $N$  respectively represent SST anomalies at the  $i$ th time step and data length of the monthly time series while the subscript  $k$  denotes the order of the statistical moment.

Considering the skewness is normalized by the cube of standard deviation, its time-varying changes relative to the control simulation can be linearly decomposed into changes related to  $m_2$  and  $m_3$  with the following Taylor expansion (only using first-order terms):

$$\Delta\gamma = -\frac{3}{2} \frac{m_3^{PD}}{m_2^{3/2} m_3} \times \Delta m_2 + \frac{m_3^{PD}}{m_2^{3/2}} \times \Delta m_3 \quad (2)$$



where an over-bar represents the long-term mean of related quantities in the PD control simulation, and the  $\Delta$  symbol indicates a relative change on this reference basis.

### Mixed layer heat budget

To investigate the physical causes of the SST variance and skewness change, an ocean mixed layer heat budget analysis in partial flux form is utilized<sup>70</sup>:

$$\frac{\partial T}{\partial t} = \frac{Q}{\rho C_p H_{\text{mid}}} - \left( \frac{\partial(\overline{uT})}{\partial x} + \frac{\partial(\overline{vT})}{\partial y} \right) + \frac{\overline{WT}_{\text{sub}}}{H_{\text{mid}}} - \left( u \frac{\partial \overline{T}}{\partial x} + v \frac{\partial \overline{T}}{\partial y} + w \frac{\partial \overline{T}}{\partial z} \right) - \left( u \frac{\partial \Delta T}{\partial x} + v \frac{\partial \Delta T}{\partial y} + w \frac{\partial \Delta T}{\partial z} \right) \quad (3)$$

The variables  $T$ ,  $u$ ,  $v$ , and  $w$  denote mixed layer ocean temperature and ocean current velocities in zonal, meridional, and vertical directions, respectively. Variables with and without an over-bar represent background mean state and anomalies respectively.  $T_{\text{sub}}$  and  $W$  are ocean temperature anomalies and background vertical current velocity at the mixed layer base.  $Q$  denotes sea surface net heat flux anomalies into the ocean. The mixed layer is fixed at a depth of 50 m ( $H_{\text{mid}} = 50$  m) while  $\rho = 1026 \text{ kg m}^{-3}$  and  $C_p = 3996 \text{ J kg}^{-1} \text{ K}^{-1}$  are seawater density and heat capacity. The grouped six terms on the right-hand side are thermal damping by net heat flux ( $Q_{\text{net}}$ ), dynamical damping by horizontal mean circulation (DD), thermocline feedback (TH), advective feedback (ADV), and nonlinear dynamical heating (NDH), respectively. On this basis, the sum of the above six explicitly calculated feedback terms is referred to as the net growth rate (GR).

### Asymmetric coupling strength

To separate El Niño and La Niña's changes, we performed ENSO phase-dependent asymmetric linear regressions<sup>71</sup> to evaluate their changes in SST-feedback coupling strength:

$$F = \begin{cases} a_{\text{El}} \times \text{SST}_{\text{ECP}} + \text{resid}_{\text{El}} & (\text{SST}_{\text{ECP}} > 0) \\ a_{\text{La}} \times \text{SST}_{\text{ECP}} + \text{resid}_{\text{La}} & (\text{SST}_{\text{ECP}} < 0) \end{cases} \quad (4)$$

where  $F$  and  $\text{SST}_{\text{ECP}}$  represent each feedback on the right-hand side of Eq. (3) and area-averaged SST anomalies over the central-to-eastern equatorial Pacific ( $90^\circ\text{--}180^\circ\text{W}$ ,  $5^\circ\text{S}\text{--}5^\circ\text{N}$ ) that cover ENSO's main activity center, respectively.  $\text{resid}$  represents an ENSO-unrelated feedback component and is not analyzed in our study.  $a$  represent each feedback's linear coupling strength with ENSO SST and is estimated in a 31-year moving window. In each window, the  $\text{SST}_{\text{ECP}}$  was normalized first to avoid possible influences from the time-varying change in ENSO intensity. The "El" and "La" suffixes represent El Niño and La Niña phases, respectively. The ENSO-phase dependent regression analysis is also applied to reveal other asymmetric features of ENSO, such as the SST's spatial pattern.

### DATA AVAILABILITY

The ERSSTv5 reanalysis is freely available at <https://psl.noaa.gov/data/gridded/data.noaa.ersst.v5.html>. The model data used in this study is publicly available at <https://figshare.com/s/b6d4686e75ecf76331f5>.

### CODE AVAILABILITY

The code used in this study is available from the corresponding author upon request.

Received: 15 May 2023; Accepted: 7 August 2023;  
Published online: 15 August 2023

### REFERENCES

1. McPhaden, M. J., Zebiak, S. E. & Glantz, M. H. ENSO as an integrating concept in earth science. *Science (1979)* **314**, 1740–1745 (2006).

- Neelin, J. D. et al. ENSO theory. *J. Geophys Res Oceans* **103**, 14261–14290 (1998).
- Taschetto, A. S. et al. *El Niño Southern Oscillation In A Changing Climate* 1st edn, 309–335 (American Geophysical Union, 2020).
- An, S.-I. A review of interdecadal changes in the nonlinearity of the El Niño–Southern Oscillation. *Theor. Appl. Climatol.* **97**, 29–40 (2009).
- Cai, W., van Rensch, P., Cowan, T. & Sullivan, A. Asymmetry in ENSO teleconnection with regional rainfall, its multidecadal variability, and impact. *J. Clim.* **23**, 4944–4955 (2010).
- Planton, Y. Y., Vialard, J., Guilyardi, E., Lengaigne, M. & McPhaden, M. J. The asymmetric influence of ocean heat content on ENSO predictability in the CNRM-CM5 coupled general circulation model. *J. Clim.* <https://doi.org/10.1175/JCLI-D-20-0633.1> (2021)
- Timmermann, A. et al. El Niño–Southern Oscillation complexity. *Nature* **559**, 535–545 (2018).
- Cai, W. et al. Antarctic shelf ocean warming and sea ice melt affected by projected El Niño changes. *Nat. Clim. Change* **13**, 235–239 (2023).
- Wang, G. et al. Future Southern Ocean warming linked to projected ENSO variability. *Nat. Clim. Change* **12**, 649–654 (2022).
- Liu, C., Zhang, W., Jin, F., Stuecker, M. F. & Geng, L. Equatorial origin of the observed tropical Pacific quasi-decadal variability from ENSO nonlinearity. *Geophys. Res. Lett.* **49**, e2022GL097903 (2022).
- Hayashi, M., Jin, F.-F. & Stuecker, M. F. Dynamics for El Niño–La Niña asymmetry constrain equatorial-Pacific warming pattern. *Nat. Commun.* **11**, 4230 (2020).
- Jin, F.-F., An, S.-I., Timmermann, A. & Zhao, J. Strong El Niño events and nonlinear dynamical heating. *Geophys. Res. Lett.* **30**, 1120 (2003).
- An, S.-I. & Jin, F.-F. Nonlinearity and asymmetry of ENSO. *J. Clim.* **17**, 2399–2412 (2004).
- Su, J. et al. Causes of the El Niño and La Niña Amplitude Asymmetry in the Equatorial Eastern Pacific. *J. Clim.* **23**, 605–617 (2010).
- Hayashi, M. & Jin, F. Subsurface nonlinear dynamical heating and ENSO asymmetry. *Geophys. Res. Lett.* **44**, 12,427–12,435 (2017).
- Kang, I.-S. & Kug, J.-S. El Niño and La Niña sea surface temperature anomalies: asymmetry characteristics associated with their wind stress anomalies. *J. Geophys. Res.* **107**, 4372 (2002).
- Choi, K.-Y., Vecchi, G. A. & Wittenberg, A. T. ENSO transition, duration, and amplitude asymmetries: role of the nonlinear wind stress coupling in a conceptual model. *J. Clim.* **26**, 9462–9476 (2013).
- An, S.-I. & Kim, J.-W. Role of nonlinear ocean dynamic response to wind on the asymmetrical transition of El Niño and La Niña. *Geophys. Res. Lett.* **44**, 393–400 (2017).
- Im, S.-H., An, S.-I., Kim, S. T. & Jin, F.-F. Feedback processes responsible for El Niño–La Niña amplitude asymmetry. *Geophys. Res. Lett.* **42**, 5556–5563 (2015).
- Guan, C., McPhaden, M. J., Wang, F. & Hu, S. Quantifying the role of oceanic feedbacks on ENSO asymmetry. *Geophys. Res. Lett.* **46**, 2140–2148 (2019).
- Kim, W., Cai, W. & Kug, J.-S. Migration of atmospheric convection coupled with ocean currents pushes El Niño to extremes. *Geophys. Res. Lett.* **42**, 3583–3590 (2015).
- Cai, W. et al. Increasing frequency of extreme El Niño events due to greenhouse warming. *Nat. Clim. Change* **4**, 111–116 (2014).
- Bellenger, H., Guilyardi, E., Leloup, J., Lengaigne, M. & Vialard, J. ENSO representation in climate models: from CMIP3 to CMIP5. *Clim. Dyn.* **42**, 1999–2018 (2014).
- Hoerling, M. P., Kumar, A. & Zhong, M. El Niño, La Niña, and the nonlinearity of their teleconnections. *J. Clim.* **10**, 1769–1786 (1997).
- Jin, F.-F., Lin, L., Timmermann, A. & Zhao, J. Ensemble-mean dynamics of the ENSO recharge oscillator under state-dependent stochastic forcing. *Geophys. Res. Lett.* **34**, L03807 (2007).
- Vialard, J. et al. A model study of oceanic mechanisms affecting equatorial Pacific sea surface temperature during the 1997–98 El Niño. *J. Phys. Oceanogr.* **31**, 1649–1675 (2001).
- An, S.-I. Interannual variations of the tropical ocean instability wave and ENSO. *J. Clim.* **21**, 3680–3686 (2008).
- Wang, C. et al. Equatorial submesoscale eddies contribute to the asymmetry in ENSO amplitude. *Geophys. Res. Lett.* **50**, e2022GL101352 (2023).
- Timmermann, A. & Jin, F.-F. Phytoplankton influences on tropical climate. *Geophys. Res. Lett.* **29**, 19–4 (2002).
- Xue, A., Zhang, W., Boucharel, J. & Jin, F.-F. Anomalous Tropical Instability Wave activity hindered the development of the 2016/2017 La Niña. *J. Clim.* <https://doi.org/10.1175/JCLI-D-20-0399.1> (2021)
- Zhang, T. & Sun, D.-Z. ENSO asymmetry in CMIP5 models. *J. Clim.* **27**, 4070–4093 (2014).
- Zhao, Y. & Sun, D.-Z. ENSO asymmetry in CMIP6 models. *J. Clim.* **35**, 5555–5572 (2022).
- Ineson, S. et al. ENSO amplitude asymmetry in met office hadley centre climate models. *Front. Clim.* **3**, 789869 (2021).

34. Chen, H.-C., Jin, F.-F., Zhao, S., Wittenberg, A. T. & Xie, S. ENSO dynamics in the E3SM-1-0, CESM2, and GFDL-CM4 Climate Models. *J. Clim.* <https://doi.org/10.1175/JCLI-D-21-0355.1> (2021)
35. Bayr, T. et al. Mean-state dependence of ENSO atmospheric feedbacks in climate models. *Clim. Dyn.* **50**, 3171–3194 (2018).
36. Sun, Y., Wang, F. & Sun, D.-Z. Weak ENSO asymmetry due to weak nonlinear air–sea interaction in CMIP5 climate models. *Adv. Atmos. Sci.* **33**, 352–364 (2016).
37. Bayr, T. et al. Error compensation of ENSO atmospheric feedbacks in climate models and its influence on simulated ENSO dynamics. *Clim. Dyn.* **53**, 155–172 (2019).
38. Cai, W. et al. Increased ENSO sea surface temperature variability under four IPCC emission scenarios. *Nat. Clim. Change* **12**, 228–231 (2022).
39. Wang, B. et al. Historical change of El Niño properties sheds light on future changes of extreme El Niño. *Proc. Natl Acad. Sci. USA* **116**, 22512–22517 (2019).
40. Yang, Y.-M., Park, J.-H., An, S.-I., Wang, B. & Luo, X. Mean sea surface temperature changes influence ENSO-related precipitation changes in the mid-latitudes. *Nat. Commun.* **12**, 1495 (2021).
41. Cai, W. et al. Increased variability of eastern Pacific El Niño under greenhouse warming. *Nature* **564**, 201–206 (2018).
42. Kohyama, T., Hartmann, D. L. & Battisti, D. S. Weakening of nonlinear ENSO under global warming. *Geophys. Res. Lett.* **45**, 8557–8567 (2018).
43. Ham, Y.-G. A reduction in the asymmetry of ENSO amplitude due to global warming: the role of atmospheric feedback. *Geophys. Res. Lett.* **44**, 8576–8584 (2017).
44. An, S., Tziperman, E., Okumura, Y. M. & Li, T. *El Niño Southern Oscillation in a Changing Climate*. p. 153–172 (John Wiley & Sons, Inc, 2020).
45. Samanta, A. et al. Physical climate response to a reduction of anthropogenic climate forcing. *Earth Interact.* **14**, 1–11 (2010).
46. Wu, P., Ridley, J., Pardaens, A., Levine, R. & Lowe, J. The reversibility of CO<sub>2</sub> induced climate change. *Clim. Dyn.* **45**, 745–754 (2015).
47. Chadwick, R., Wu, P., Good, P. & Andrews, T. Asymmetries in tropical rainfall and circulation patterns in idealised CO<sub>2</sub> removal experiments. *Clim. Dyn.* **40**, 295–316 (2013).
48. Wu, P., Wood, R., Ridley, J. & Lowe, J. Temporary acceleration of the hydrological cycle in response to a CO<sub>2</sub> rampdown. *Geophys. Res. Lett.* **37**, L12705 (2010).
49. Boucher, O. et al. Reversibility in an Earth System model in response to CO<sub>2</sub> concentration changes. *Environ. Res. Lett.* **7**, 024013 (2012).
50. Cao, L., Bala, G. & Caldeira, K. Why is there a short-term increase in global precipitation in response to diminished CO<sub>2</sub> forcing? *Geophys. Res. Lett.* **38**, L06703 (2011).
51. An, S. et al. Global cooling hiatus driven by an AMOC overshoot in a carbon dioxide removal scenario. *Earths Future* **9**, e2021EF002165 (2021).
52. Kug, J.-S. et al. Hysteresis of the intertropical convergence zone to CO<sub>2</sub> forcing. *Nat. Clim. Change* **12**, 47–53 (2021).
53. Burgers, G. & Stephenson, D. B. The “normality” of El Niño. *Geophys. Res. Lett.* **26**, 1027–1030 (1999).
54. DiNezio, P. N., Deser, C., Okumura, Y. & Karspeck, A. Predictability of 2-year La Niña events in a coupled general circulation model. *Clim. Dyn.* **49**, 4237–4261 (2017).
55. Wu, X., Okumura, Y. M. & DiNezio, P. N. What controls the duration of El Niño and La Niña Events? *J. Clim.* **32**, 5941–5965 (2019).
56. Kim, J.-W. & Yu, J.-Y. Single- and multi-year ENSO events controlled by pantropical climate interactions. *NPJ Clim. Atmos. Sci.* **5**, 88 (2022).
57. Jin, F.-F. & An, S.-I. Thermocline and zonal advective feedbacks within the equatorial ocean recharge oscillator model for ENSO. *Geophys Res Lett.* **26**, 2989–2992 (1999).
58. Liu, C. et al. Hysteresis of the El Niño–Southern Oscillation to CO<sub>2</sub> forcing. *Sci. Adv.* **9**, eadh8442 (2023).
59. Jin, F.-F. An equatorial ocean recharge paradigm for ENSO. part I: conceptual model. *J. Atmos. Sci.* **54**, 811–829 (1997).
60. Jin, F.-F. An equatorial ocean recharge paradigm for ENSO. Part II: a stripped-down coupled model. *J. Atmos. Sci.* **54**, 830–847 (1997).
61. Santoso, A., McPhaden, M. J. & Cai, W. The defining characteristics of ENSO extremes and the strong 2015/2016 El Niño. *Rev. Geophys.* **55**, 1079–1129 (2017).
62. Huang, P. & Xie, S.-P. Mechanisms of change in ENSO-induced tropical Pacific rainfall variability in a warming climate. *Nat. Geosci.* **8**, 922–926 (2015).
63. Yan, Z. et al. Eastward shift and extension of ENSO-induced tropical precipitation anomalies under global warming. *Sci. Adv.* **6**, eaax4177 (2020).
64. Held, I. M. & Soden, B. J. Robust responses of the hydrological cycle to global warming. *J. Clim.* **19**, 5686–5699 (2006).
65. Oh, H. et al. Contrasting hysteresis behaviors of northern hemisphere land monsoon precipitation to CO<sub>2</sub> pathways. *Earths Future* **10**, e2021EF002623 (2022).
66. Callahan, C. W. et al. Robust decrease in El Niño/Southern Oscillation amplitude under long-term warming. *Nat. Clim. Change* **11**, 752–757 (2021).
67. Hurrell, J. W. et al. The community earth system model: a framework for collaborative research. *Bull. Am. Meteorol. Soc.* **94**, 1339–1360 (2013).
68. Huang, B. et al. Extended reconstructed sea surface temperature, version 5 (ERSSTv5): upgrades, validations, and intercomparisons. *J. Clim.* **30**, 8179–8205 (2017).
69. Frierson, D. M. W. & Hwang, Y.-T. Extratropical influence on ITCZ shifts in slab ocean simulations of global warming. *J. Clim.* **25**, 720–733 (2012).
70. An, S.-I., Jin, F.-F. & Kang, I.-S. The role of zonal advection feedback in phase transition and growth of ENSO in the Cane-Zebiak Model. *J. Meteorol. Soc. Jpn Ser. II* **77**, 1151–1160 (1999).
71. Frankignoul, C. & Kwon, Y. On the statistical estimation of asymmetrical relationship between two climate variables. *Geophys. Res. Lett.* **49**, e2022GL100777 (2022).

## ACKNOWLEDGEMENTS

We are grateful to two anonymous reviewers for their insightful and valuable feedback that improved the quality of this manuscript. This work was supported by a National Research Foundation of Korea (NRF) grant funded by the Korean government (MSIT) (NRF-2018R1A5A1024958). Model simulation and data transfer were supported by the National Supercomputing Center with supercomputing resources including technical support (KSC-2021-CHA-0030), the National Center for Meteorological Supercomputer of the Korea Meteorological Administration (KMA), and the Korea Research Environment Open Network (KREONET), respectively. M.F.S. was supported by NSF grant AGS-2141728. This is an IPRC publication 1608 and SOEST contribution 11706. X.Y. was supported by the National Natural Science Foundation of China (42205052).

## AUTHOR CONTRIBUTIONS

C.L., S.I.A., and F.F.J. conceived the idea. C.L. and S.I.A. designed the study. C.L. conducted the analysis, wrote the initial draft of the manuscript, and produced all figures. S.I.A. guided the research and oversaw the project. J. S. conducted the Earth System Model Experiment. All authors contributed to the interpretation of the results and improvement of the manuscript.

## COMPETING INTERESTS

The authors declare no competing interests.

## ADDITIONAL INFORMATION

**Supplementary information** The online version contains supplementary material available at <https://doi.org/10.1038/s41612-023-00448-6>.

**Correspondence** and requests for materials should be addressed to Soon-Il An.

**Reprints and permission information** is available at <http://www.nature.com/reprints>

**Publisher's note** Springer Nature remains neutral with regard to jurisdictional claims in published maps and institutional affiliations.



**Open Access** This article is licensed under a Creative Commons Attribution 4.0 International License, which permits use, sharing, adaptation, distribution and reproduction in any medium or format, as long as you give appropriate credit to the original author(s) and the source, provide a link to the Creative Commons license, and indicate if changes were made. The images or other third party material in this article are included in the article's Creative Commons license, unless indicated otherwise in a credit line to the material. If material is not included in the article's Creative Commons license and your intended use is not permitted by statutory regulation or exceeds the permitted use, you will need to obtain permission directly from the copyright holder. To view a copy of this license, visit <http://creativecommons.org/licenses/by/4.0/>.